JOURNAL OF SYNCHROTRON RADIATION

ISSN 1600-5775

Pulse-resolved intensity measurements at a hard X-ray FEL using semi-transparent diamond detectors

Thomas Roth,[a]*‡ Wolfgang Freund,[a] Ulrike Boesenberg,[a] Gabriella Carini,[b] Sanghoon Song,[b] Gwenaëlle Lefeuvre,[c] Alexander Goikhman,[d] Martin Fischer,[e] Matthias Schreck,[e] Jan Grünert[a] and Anders Madsen[a]*

[a]European X-ray Free-Electron Laser Facility, Holzkoppel 4, 22869 Schenefeld, Germany, [b]Linac Coherent Light Source, SLAC National Accelerator Laboratory, Menlo Park, CA 94025, USA, [c]Micron Semiconductors Ltd, 85 Marlborough Road, Lancing, UK, [d]Immanuel Kant Baltic Federal University, Nevskogo 14, Kaliningrad 236041, Russian Federation, and [e]Institut für Physik, Universität Augsburg, Universitätsstrasse 1, 86159 Augsburg, Germany.
*Correspondence e-mail: thomas.roth@esrf.eu, anders.madsen@xfel.eu

Received 2 June 2017
Accepted 16 October 2017

Edited by G. Grübel, HASYLAB at DESY, Germany

‡ Present address: European Synchrotron Radiation Facility, Grenoble, France.

Keywords: XFEL; diamond detector; X-ray intensity measurement.

Solid-state ionization chambers are presented based on thin diamond crystals that allow pulse-resolved intensity measurements at a hard X-ray free-electron laser (FEL), up to the 4.5 MHz repetition rate that will become available at the European XFEL. Due to the small X-ray absorption of diamond the thin detectors are semi-transparent which eases their use as non-invasive monitoring devices in the beam. FELs are characterized by strong pulse-to-pulse intensity fluctuations due to the self-amplified spontaneous emission (SASE) process and in many experiments it is mandatory to monitor the intensity of each individual pulse. Two diamond detectors with different electrode materials, beryllium and graphite, were tested as intensity monitors at the XCS endstation of the Linac Coherent Light Source (LCLS) using the pink SASE beam at 9 keV. The performance is compared with LCLS standard monitors that detect X-rays backscattered from thin SiN foils placed in the beam. The graphite detector can also be used as a beam position monitor although with rather coarse resolution.

1. Introduction

X-ray free-electron lasers (FELs) deliver X-ray pulses of a few tens of femtoseconds duration with extreme peak intensities. The intensity varies from pulse to pulse due to the stochastic nature of the self-amplified spontaneous emission (SASE) process that is responsible for the intense laser-like X-ray pulses (Kondratenko & Saldin, 1980; Bonifacio *et al.*, 1984). In order to quantify the intensity of every pulse at various positions along the beam path it is necessary to employ fast and highly transparent intensity detectors. High transparency ensures a minimum attenuation of the beam as it travels to the experiment even with several detectors inserted simultaneously. In this respect up to 10 µm-thick Si or 100 µm-thick diamond is acceptable for X-ray energies above 5 keV. A small X-ray absorption cross section as encountered in low-Z materials also reduces radiation-induced damage of the detector caused by ablation (Bionta, 2000; London *et al.*, 2001; Hau-Riege *et al.*, 2007, 2010; Koyama *et al.*, 2013*a*). At the European X-ray Free Electron Laser (Altarelli, 2015), the pulse-to-pulse spacing inside a pulse train is 220 ns (4.5 MHz). An upgrade of the Linac Coherent Light Source (LCLS) (Emma *et al.*, 2014) plans for equidistant pulses with a repetition rate as high as 1 MHz. Often, diode-type detectors are considered as RC circuits with a time constant of $\tau = RC$ where R and C are the detector resistance and capacitance, respectively. Obviously, τ needs to be much faster than 220 ns for

pulse-resolved intensity measurements at the European XFEL.

Gas detectors are less efficient at high photon energies but can in principle be used as non-invasive intensity monitors (Hau-Riege *et al.*, 2008; Tiedtke *et al.*, 2008). However, they require gas exchange piping and entrance/exit windows, or long differential pumping sections which are not always possible to implement. Detectors relying on measurement of radiation scattered off thin foils inserted into the beam have also been employed for this purpose (Tono *et al.*, 2011; Feng *et al.*, 2011; Herrmann *et al.*, 2014; Kudo *et al.*, 2012). However, the use of scattered radiation has the disadvantage that the differential scattering cross section is highly energy-dependent so it is difficult to perform a good calibration over the entire spectrum and obtain absolute intensity values. Compared with other solid-state detector materials, diamond has the advantage of a very high thermal conductivity which will help dissipate the average absorbed power. Furthermore, the threshold for single-pulse ablation is high. Diamond is thus the detector material of choice for FEL applications. However, such solid-state detectors require electrodes on both sides of the absorbing sensor material that the X-ray beam also will traverse. The choice of electrode material will be discussed later.

Single-crystalline chemical vapor deposited (scCVD) diamond detectors have been used previously at synchrotron sources, either as intensity monitors (Morse *et al.*, 2007; De Sio *et al.*, 2007; Keister & Smedley, 2009) or as quadrant beam position monitors (BPMs) (Morse *et al.*, 2007, 2010; Bohon *et al.*, 2010; Keister *et al.*, 2011; Desjardins *et al.*, 2014). In addition, homogeneous BPMs using electrodes on each crystal edge (Pomorski *et al.*, 2009) are available. The rapid speed of diamond detectors was already exploited to detect intensity and position at the bunch frequency of a synchrotron X-ray source (Morse *et al.*, 2010; Antonelli *et al.*, 2013). Recently, pixelated diamond detectors have been developed to serve as semi-transparent two-dimensional beam imagers (Zhou *et al.*, 2015).

Here, we discuss the use of diamond as in-line semi-transparent intensity monitors or BPMs at a hard X-ray FEL. FELs are fully transverse coherent sources so electrode edges or any other features cannot be allowed over the beam footprint because this would lead to interference patterns in the transmitted beam. Moreover, similar to the detector material, materials as light as possible are favored for the electrodes in order to avoid ablation and consequently the detectors discussed here are only using materials with $Z \leq 6$. We thus present two diamond detectors with beryllium and graphite as electrode materials.

2. Boundary conditions

2.1. Absorption

To limit absorption, a detector as thin as possible is preferred although the signal strength is proportional to the detector thickness in the thin detector limit. X-ray pulse intensities at XFELs are sufficiently high to give a strong detector signal even if the absorption is only 1% or below. Si detectors are available down to 5 µm (Fuchs *et al.*, 2008) and diamond detectors are now reaching thicknesses down to 20 µm (Shimaoka *et al.*, 2016) for large areas and even less if the diamond crystal is thinned down over a limited region (Desjardins *et al.*, 2014). However, already at a thickness of 40 µm, diamond absorbs less than 22% for energies above 5 keV (see Fig. 1, top), equivalent to 5 µm of Si. Higher transparency also reduces the amount of heat generated in the detector by absorption. This can be a significant problem at high-repetition-rate XFELs: for example, one absorbs up to 6.3 W of the pink beam at 5 keV at the European XFEL with a transmission T of 77.5% in a 40 µm-thick diamond crystal.

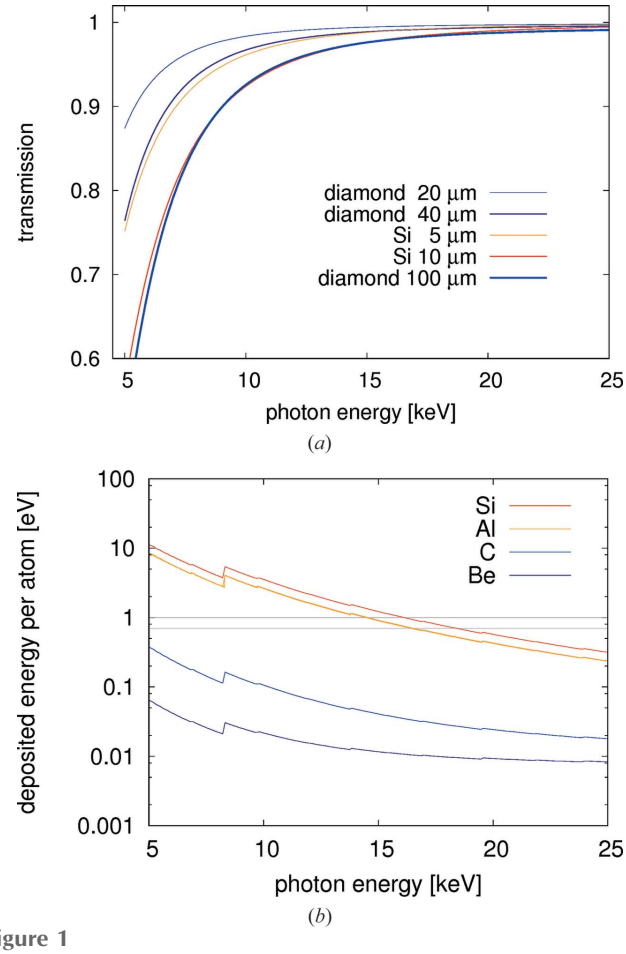

Figure 1
Top: absorption in Si and diamond as a function of photon energy. Bottom: energy deposited per atom and per pulse for different materials, calculated for a detector placed 30 cm upstream of the sample position at the MID station of the European XFEL in a pink SASE beam. The beam size is calculated assuming one of the standard focusing schemes available at MID (collimated, then focused) (Madsen *et al.*, 2013). The ablation (graphitization) threshold is at approximately 1 eV (0.7 eV) absorbed energy per atom and per pulse. The step at around 8 keV comes from different operation modes at the European XFEL.

2.2. Diamond ablation and graphitization thresholds

Single XFEL pulses can be intense enough to remove solid matter almost instantaneously through the creation of a

plasma, an effect denoted ablation (Hau-Riege *et al.*, 2007; Koyama *et al.*, 2013*b*). As a rule of thumb, the critical threshold for single-shot ablation is reached when the energy absorbed per atom, $\eta = \sigma_{abs} NE/A$, is larger than 1 eV. Here N, E and A are the number of photons per pulse, the photon energy and the beam area, respectively. The larger the atomic number Z of the absorbing material, the higher the absorption cross section σ_{abs} and the lower the required beam flux for ablation. Low-Z detector and electrode materials are therefore desired. Electrodes can, for instance, be diamond-like carbon (DLC), graphite or beryllium, in order not to exceed $Z = 6$. Fig. 1 (bottom) shows calculations of η for Be, C, Al and Si in a focused beam at the Materials Imaging and Dynamics (MID) endstation of the European XFEL, 30 cm upstream of the sample position, and compares it with the approximate 1 eV atom^{-1} limit for ablation. From the figure it is obvious that when operating with diamond and beryllium there is a safety margin in the entire photon energy range, even under these extreme conditions. This is not the case for more conventional materials like silicon or aluminium.

In addition to the risk of material ablation, a particular problem for diamond is graphitization. At a lower photon flux than required for ablation, the diamond structure can be transformed into graphite or amorphous carbon by beam illumination. If the bulk of the diamond plate transforms to graphite it will lead either to a short circuit or to a change in the otherwise homogeneous electric field inside the detector leading to malfunctioning. The threshold for graphitization was calculated to be 0.7 eV atom^{-1} (Medvedev *et al.*, 2013*a*,*b*) and later confirmed in experiments (Gaudin *et al.*, 2013; Tavella *et al.*, 2017). In comparison, the critical thresholds for thermal and non-thermal melting of Si have been calculated to be 0.65 eV and 0.9 eV, respectively (Medvedev *et al.*, 2015). However, these numbers are reached at much fewer incident photons N because the absorption cross section σ_{abs} is higher for Si than for C. Hence, diamond detectors are still much favored for XFEL applications compared with Si-based devices.

2.3. European XFEL time structure and detector time constant

The European XFEL exhibits a time structure with 600 µs-long photon pulse trains that arrive at a repetition rate of 10 Hz. Inside each train a maximum of 2700 pulses are equally spaced at a frequency of 4.5 MHz, thus having 220 ns pulse-to-pulse separation. Each photon pulse has a duration $\leq$100 fs. The detector and the circuit must allow an intensity measurement of each individual photon pulse, hence requiring a time constant of the full setup $\tau_{exp} \lesssim 50$ ns, depending on the detailed shape of the signal decay (see Fig. 2).

As the drift velocities for electrons and holes in diamond at saturation are $v_{s,e} \simeq 2 \times 10^5$ m s^{-1} and $v_{s,h} \simeq 1 \times 10^5$ m s^{-1}, respectively (Wort & Balmer, 2008), the rise time of the detected signal will be very fast, typically less than 1 ns for a 40 µm-thick diamond. The signal decay time is determined by the detector and measurement circuit together. We consider the setup as an RC circuit that exhibits a time constant $\tau = RC$. Fig. 2 shows the expected time behavior of the detector current for three different time constants and at 4.5 MHz repetition rate. Ideally the signal has fully decayed before the next pulse arrives 220 ns later and, as the figure illustrates, a decay time τ of 50 ns or less is preferred.

The capacitance of the diamond detector is $C_{det} = \varepsilon_r \varepsilon_0 A/d$, where the relative permittivity of scCVD diamond is assumed to be $\varepsilon_r \simeq 5.7$ (commonly accepted value) although recent measurements might indicate a lower value of 4.6 (Fraimovitch *et al.*, 2016). A is the area of the electrodes as they define the high-electric-field region, and d is the thickness of the diamond plate. There are different contributions to the resistance: R_{tot} is obtained as the sum of the sheet resistance of the electrode material ($R_{electrode}$), the contact resistance at the interface ($R_{interface}$) between diamond and the electrodes, and the measurement circuit resistance ($R_{measure}$), often 50 Ω. The electrodes need to be as conductive as possible and electrically well connected to the bulk diamond in order to reduce the detector contribution $R_{det} = R_{electrode} + R_{interface}$. A good electrode-to-bulk connection is an ohmic contact, as opposed to a contact exhibiting a Schottky barrier, but this is difficult to achieve with metallizations on diamond (Tachibana & Glass, 1995). The final time constant τ_{exp} is

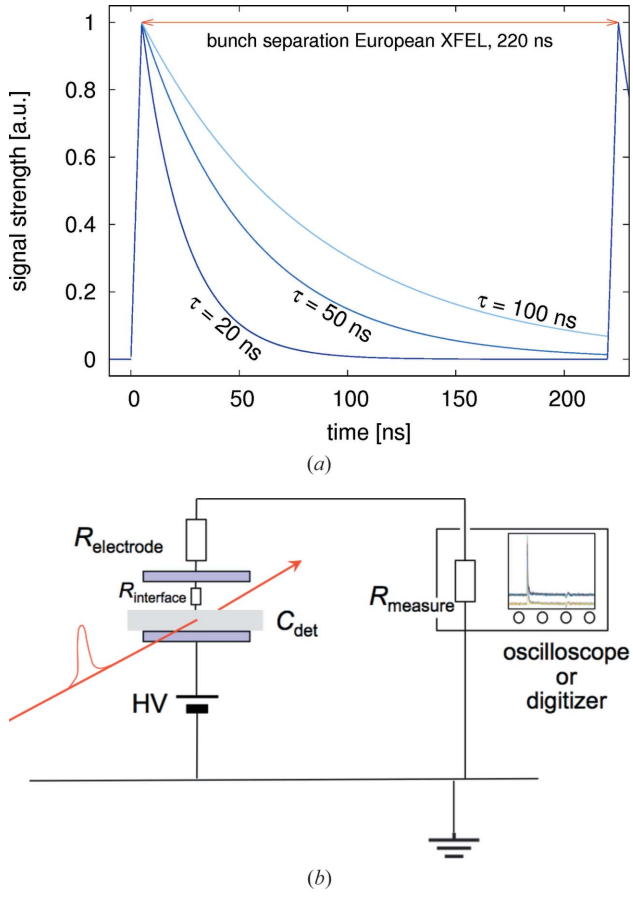

Figure 2
Top: illustration of the time constant required in order to enable detection of each pulse's intensity, separated by 220 ns at the European XFEL, and avoiding signal pile-up. Bottom: sketch of the detector visualized as an RC circuit.

$$\tau_{\rm exp} = R_{\rm tot}\, C_{\rm det} = (R_{\rm measure} + R_{\rm electrode} + R_{\rm interface})\, C_{\rm det}. \quad (1)$$

A sketch of the detector and measurement circuit is shown in Fig. 2 with the different contributions to $\tau_{\rm exp}$ indicated.

2.4. Stored and created charges

When a bias voltage $U_{\rm bias}$ is applied to a solid-state diamond detector it is charged like a capacitor. The stored charge is given by

$$Q_{\rm stored} = U_{\rm bias}\, C_{\rm det} = U_{\rm bias}\, \varepsilon_{\rm r}\varepsilon_0 (A/d). \quad (2)$$

These charges create an electric field inside the diamond sensor that allows the electron–hole pairs created by the absorbed X-rays during a photon pulse to be separated and collected. For each absorbed photon pulse, a certain number of electron–hole pairs and thus a certain charge $Q_{\rm created}$ is created. In diamond, the creation of an electron–hole pair requires about 13 eV (Pomorski *et al.*, 2005). We have thus

$$Q_{\rm created} = N(1-T)\left(\frac{E}{13\,{\rm eV}}\right) e, \quad (3)$$

where $(1-T)$ is the absorbed fraction of incoming photons, e is the elementary charge, and N is the number of photons pulse^{-1}. Ideally, the created charge is smaller than the stored charge; if not, the applied field will break down in the irradiated region and the electron–hole pairs might recombine instead of being collected at the electrode (see §2.5).

As an example, consider a 40 µm-thick diamond crystal, 10^{11} incident photons per pulse at 10 keV, 4 mm × 4 mm large electrodes and a bias voltage of 160 V. This leads to an absorption $(1-T)$ of 4% and $C_{\rm det}$ = 20 pF. We see that $Q_{\rm stored}$ = 3.2 nC is much smaller than $Q_{\rm created}$ = 490 nC. Obviously, the field will break down during the absorption of the X-ray pulse. An extra capacitor in parallel with the detector would improve the capability to store charges (Griesmayer, 2015). This will increase the time constant $\tau_{\rm exp}$ as the total capacitance grows but if $R_{\rm det}$ is sufficiently small it can be tolerated. Also, increasing the applied bias voltage increases the amount of stored charges.

2.5. Charge carrier lifetimes

Typical lifetimes of charge carriers in high-quality scCVD diamond are around 1 µs (Isberg *et al.*, 2002; Pomorski *et al.*, 2007). For heteroepitaxially grown diamond, the lifetime depends on the dislocation density which varies with growth thickness. Comparing with recent lifetime measurements of similar crystals, we expect a charge carrier lifetime of a few nanoseconds for the graphite electrode detector presented here (Mayr *et al.*, 2018). According to these data we suspect that heteroepitaxially grown crystals with lifetimes above 10 ns are within reach.

If the charge carrier lifetimes are smaller than the time constant of the measurement circuit and the created charges outnumber the stored ones, a partial recombination of created charges will occur. Adding the extra capacitor in order to increase the amount of stored charges furthermore allows the created charges to be extracted and buffered before they can recombine if the charge carrier lifetime is too small.

3. Fabrication and characterization of two diamond detectors

3.1. Be electrode detector

The diamond plate is a 4 mm × 4 mm scCVD diamond of 40 µm thickness with a thickness variation of ≤1 µm. Its surface roughness is approximately 10 nm. A 3 mm × 3 mm area on both sides of the diamond was coated with 250 nm beryllium without buffer layer, thus avoiding any high-Z material. The coating was carried out by Lebow Company, USA, after a proprietary plasma cleaning step was applied. The coating process was performed employing electron beam heated evaporation of Be; the diamond was held at room temperature. Ultrasonic wire bonding used standard AlSi wire (99% Al content) to connect the electrodes to a ceramic printed circuit board (PCB), see Fig. 3. The theoretical sheet resistance of a 250 nm-thick Be electrode is 1 Ω square^{-1} and the capacitance of the diamond plate is calculated as $C_{\rm det}$ = 11 pF. Taking the 50 Ω readout circuit into account, a time constant of $\tau_{\rm exp}$ = 0.6 ns is hence expected if the Be–C interface resistance $R_{\rm interface}$ is negligible. The detector signal did not show such a fast response in any of the tests which could be explained by the effects of $Q_{\rm created} > Q_{\rm stored}$ and/or by a non-negligible interface resistance which would thus increase $\tau_{\rm exp}$. Interface effects between diamond and Be have to be investigated more closely in the future in order to optimize the detector design.

3.1.1. Alpha-particle tests. The quality of the Be-electrode detector in terms of energy resolution was tested *via* irradiation of the assembled detector with a ^{241}Am α-particle source. The α-particles have an energy of 5.486 MeV and a penetration range of ∼13 µm into diamond. The collected charges are integrated for each detected α-particle and this signal is added to a multi-channel analyzer (MCA) histogram, shown in Fig. 4. At a bias voltage higher than about 10 V (0.25 V µm^{-1}), all created electron–hole pairs are collected, similar to other

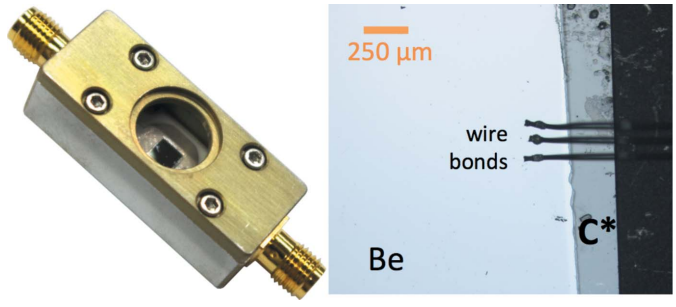

Figure 3
Left: photograph of the assembled Be-coated diamond detector with the PCB and the square diamond plate inside in the center. Right: microscope image of the wire bonds connecting the Be electrode (bright) on the diamond substrate (gray) to the PCB (black).

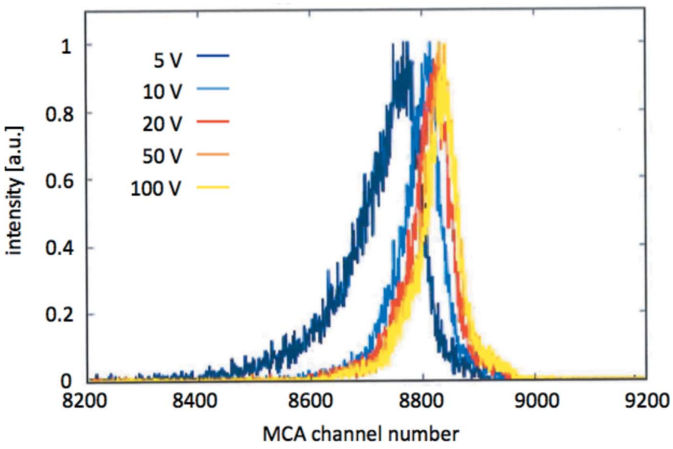

Figure 4
Histogram of collected signal heights using a ^{241}Am α-particle source and applying different bias voltages.

detector tests reported in the literature (see, for example, Morse *et al.*, 2010).

To determine the detector's energy resolution from the injection of α-particles, the histograms shown in Fig. 4 must be deconvoluted with a response function (not shown) that was measured *via* charge injection into the measurement circuit. We find that, starting from a bias voltage of 20 V, the resolution of the detector is constant and about 0.6% FWHM. This proves the good scCVD diamond quality that is fully compatible with quantitative X-ray intensity measurements.

3.2. Graphite electrode detector

This detector is based on a single-crystalline diamond plate produced *via* heteroepitaxial growth on an iridium substrate, manufactured at the University of Augsburg. Heteroepitaxial growth on wafer-size substrates facilitates the synthesis of large diamond plates (Schreck, 2014; Stehl *et al.*, 2013). After a thickness of approximately 30 µm has been reached, the diamond layer becomes single crystalline, *i.e.* the initially present closed grain boundary network has vanished. In order to obtain the best crystalline quality by a reduction of the dislocation density, growth is continued for many hundreds of micrometers but only the upper region is used for the detector. The lower region is removed by laser cutting and the top plate (7 mm × 7 mm) further thinned down by etching. The final diamond crystal thickness is 90 µm. The graphite electrodes have been produced subsequently *via* illumination of the diamond crystal by a high-energy carbon ion-beam through a mask (4 mm × 4 mm), followed by an annealing procedure. The carbon ion-beam bombardment results in amorphization of the surface region (about 250 nm) and leads to creation of sp^2 bonds between atoms. The annealing further enhances the graphitic bonding resulting in a low-resistivity graphitic layer (Kalish & Prawer, 1995). A carbon ion-beam is used for bombardment as this does not introduce impurities in the diamond. Alternatively, laser irradiation can also be employed to generate such graphite electrodes and is used for example in pixelated diamond detectors (Komlenok *et al.*, 2016).

The resistance of the graphite electrodes is around 100 Ω square^{-1} which is large enough to apply two electrodes per side and detect the position of the X-ray pulse *via* the difference between the measured currents. This scheme can be improved to perform perpendicular measurements of both transverse positions (two-dimensional) while still allowing a bias voltage to be applied (Pomorski *et al.*, 2009). The application of the bias voltage and signal readout to the surface of the graphite electrode was made by simple clamping using copper–beryllium springs. The detector is shown in Fig. 5. Owing to the electrode sizes and the diamond thickness, this detector has a capacitance of about $C_{\rm det}$ = 9 pF. Neglecting $R_{\rm interface}$ and using $R_{\rm measure}$ = 50 Ω, a signal decay time of $\tau_{\rm exp}$ = 1.4 ns is thus expected.

3.2.1. Homogeneity. The homogeneity and uniformity in thickness and response of the detector was tested using an X-ray beam of 0.1 mm × 0.1 mm size at the ID06 beamline of the European Synchrotron Radiation Facility (ESRF). The photon energy was 10.76 keV, selected by a Si(111) monochromator. The graphite detector was placed in between an ionization chamber and a Si p-i-n diode for normalization purposes. Three Keithley pico-ampere meters collected the time-averaged current created by the X-rays absorbed in the three detectors. The bias voltage applied to the diamond detector was 50 V. Fig. 6 shows a homogeneous transmission over the full detector area (top) as detected by the downstream Si p-i-n diode and a mostly uniform signal response of the diamond detector itself (bottom). The corner regions are brighter due to fluorescence radiation created in the copper–beryllium clamps. The three central bright spot-like regions are undesired, however. Such features are not uncommon in

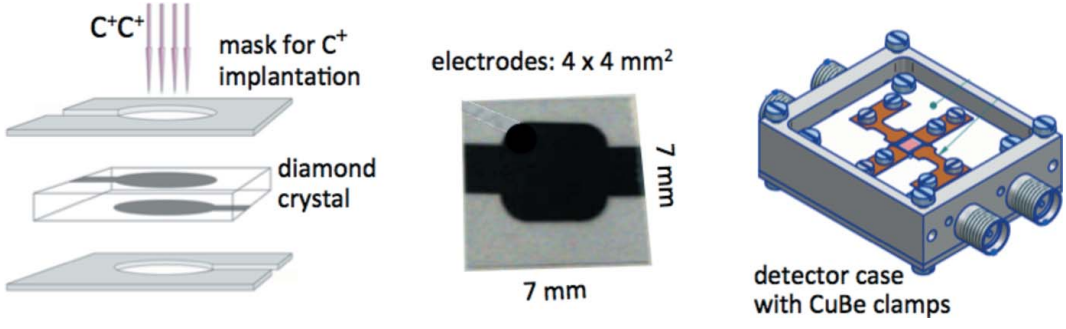

Figure 5
The diamond detector with graphite electrodes: from left to right, electrode fabrication, finished detector and housing.

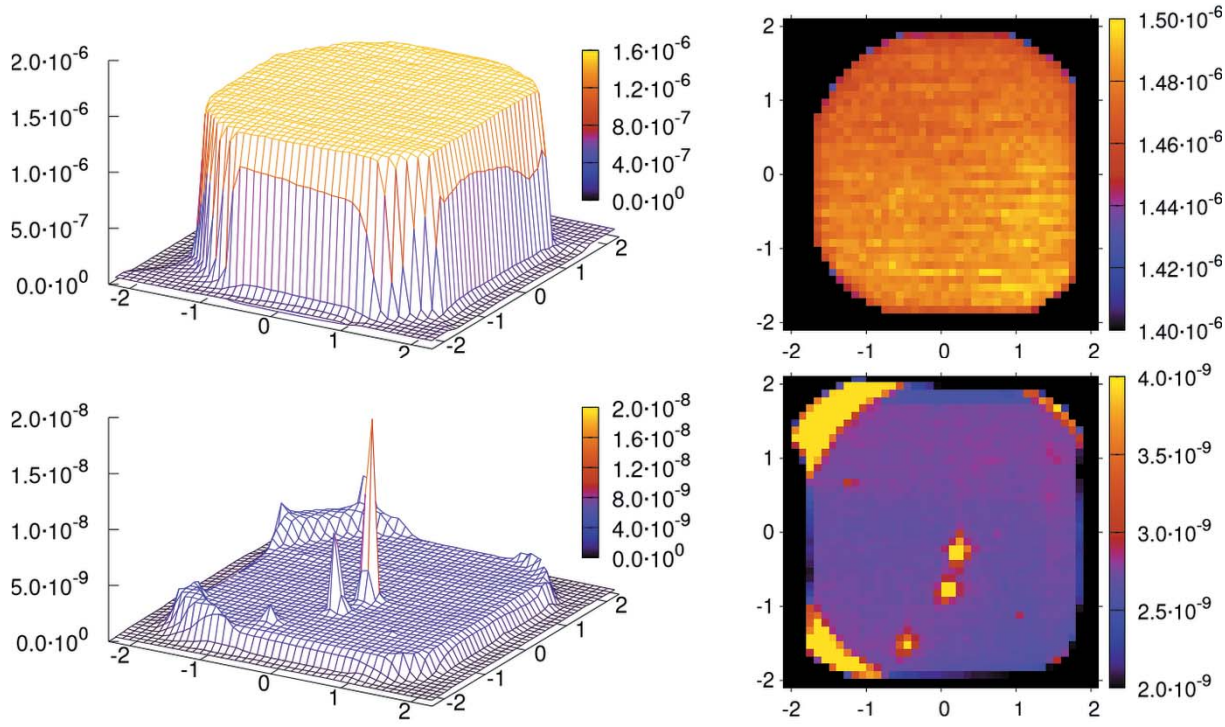

Figure 6
Top: transmission through the diamond, showing homogeneous thickness (left: three-dimensional plot; right: projection). Bottom: diamond detector response. Three hot spots are clearly visible in the response. The corner regions show higher intensity levels due to the copper clamps creating fluorescent X-rays that are absorbed by the underlying diamond. Data taken at ID06, ESRF.

scCVD diamond (Morse *et al.*, 2007) and are referred to as 'hot' defects. Here, they are giving current readings up to five times higher than experienced in the flat plateau region. The defect sizes can be up to 100 µm but other than that the response is uniform within ±3%.

4. Experimental setup at LCLS

Experiments have been performed at the XCS beamline of the LCLS (Robert *et al.*, 2013; Alonso-Mori *et al.*, 2015) in order to characterize the temporal response of the detectors in a hard X-ray FEL beam. A sketch of the setup is shown in Fig. 7. The electron bunch charge was 180 pC, the photon energy E = 9 keV, the photon pulse repetition rate 120 Hz, and the duration of individual pulses about 33 fs. The pink SASE beam passing *via* a horizontal-offset mirror reached the detector without use of any focusing optics. A slit and absorber system limited the flux to $\sim 10^{11}$ photons pulse^{-1}. All detector tests were performed in air. Downstream of the diamond detector a camera coupled to a scintillator screen (not shown in Fig. 7) allowed the transmitted beam to be imaged for alignment purposes.

In order to evaluate the linearity of the output signal coming from the diamond detectors, four other detectors installed at the XCS beamline were used for calibration. These were (i) a gas ionization chamber downstream of the undulator but upstream of the horizontal offset mirror yielding $I_{\rm gas}$, (ii) a set of four diodes detecting photons scattered off a Si_3N_4 foil (Feng *et al.*, 2011) placed 48 m upstream of the diamond detector, giving $I_{\rm array1}$, (iii) a similar set 1 m upstream of the diamond detector, giving $I_{\rm array2}$, and (iv) a single Si p-i-n diode positioned next to the diamond detector and detecting photons scattered from a Kapton window at the end of the beam pipe 20 cm upstream of the diamond detector, giving $I_{\rm Si3}$. Only one diamond detector was used at a time and aligned with the camera system.

The current signal from the diamond detectors was attenuated by up to 33 dB using passive SMA attenuators (Mini-Circuits VAT series). This allows matching the signal height to the working range of the Acqiris digitizer SC 240 that collected the detector's signal from each photon pulse at 2 GS s^{-1}, *i.e.* 0.5 ns resolution. Four untreated signal traces from the graphite diamond detector are shown in the inset of Fig. 7.

5. Results

5.1. Signal shape and duration

Eight thousand pulse traces were recorded for both diamond detectors, together with the integrated signals of the Si reference detectors. The right-hand column of Fig. 8 shows the integrated signals for 5000 X-ray pulses: in blue, the diamond detectors are shown (top: Be electrode detector; bottom: graphite electrode detector); in red, the Si p-i-n diode signal $I_{\rm Si3}$. A large signal variation from pulse to pulse is visible, caused by the strong SASE intensity fluctuations. The experimental conditions have been similar for both detectors

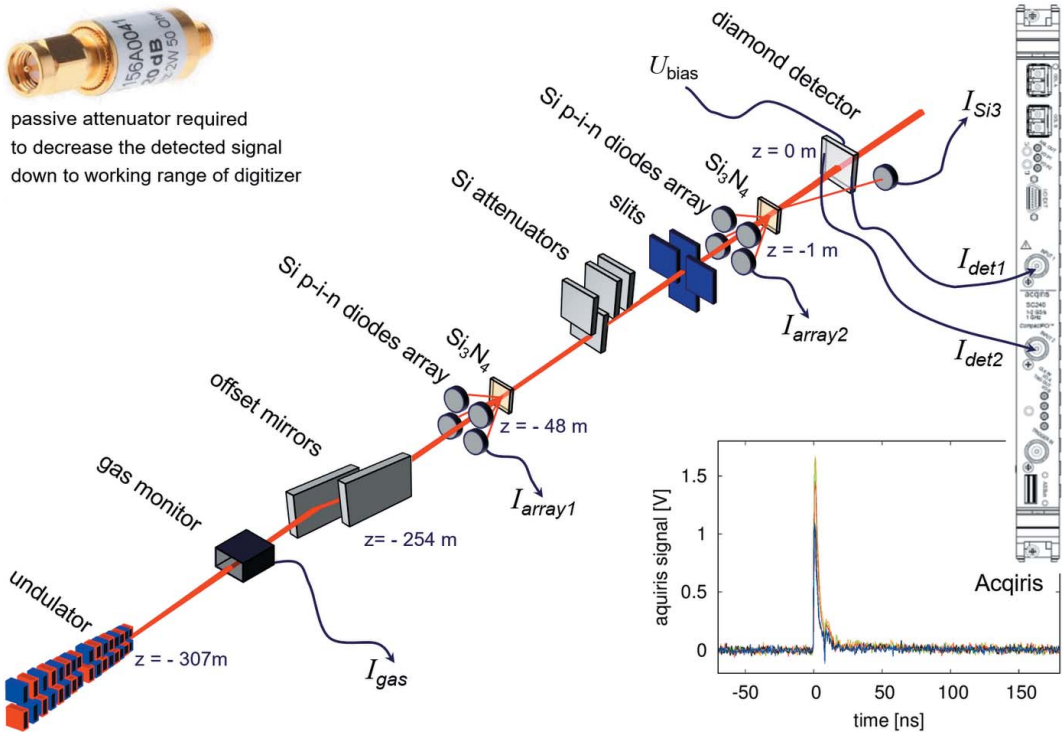

Figure 7
Beamline layout of the detector test experiments at LCLS. The principal components are shown with the used intensity monitors and their positions relative to the diamond detector (z = 0). To the right is shown the Acqiris digitizer and four signals measured with the graphite electrode diamond detector.

with no attenuation of the X-ray beam and −33 dB attenuation of the detector signal prior to connecting to the fast digitizer. Only the slit settings have been slightly different (0.6 mm × 0.1 mm for the Be detector and 0.2 mm × 0.2 mm for the graphite detector) and the bias voltage was 160 V and 100 V for the Be and graphite detectors, respectively. Fig. 8, left column, shows selected individual signal traces for the Be electrode detector (top) and the graphite detector (bottom), representing a very weak, a weak, a moderate, a strong and a very strong SASE pulse out of the 5000 pulses shown on the right. For both diamond detectors, dips can be observed at t = 8 ns and 15 ns in the traces recorded by the digitizer. These features are likely caused by a slight impedance mismatch between detector and acquisition electronics leading to a signal reflection. An optimization on this point is foreseen in the future detector development but it has little effect on the data.

The Be electrode detector signals decay much slower than the expected

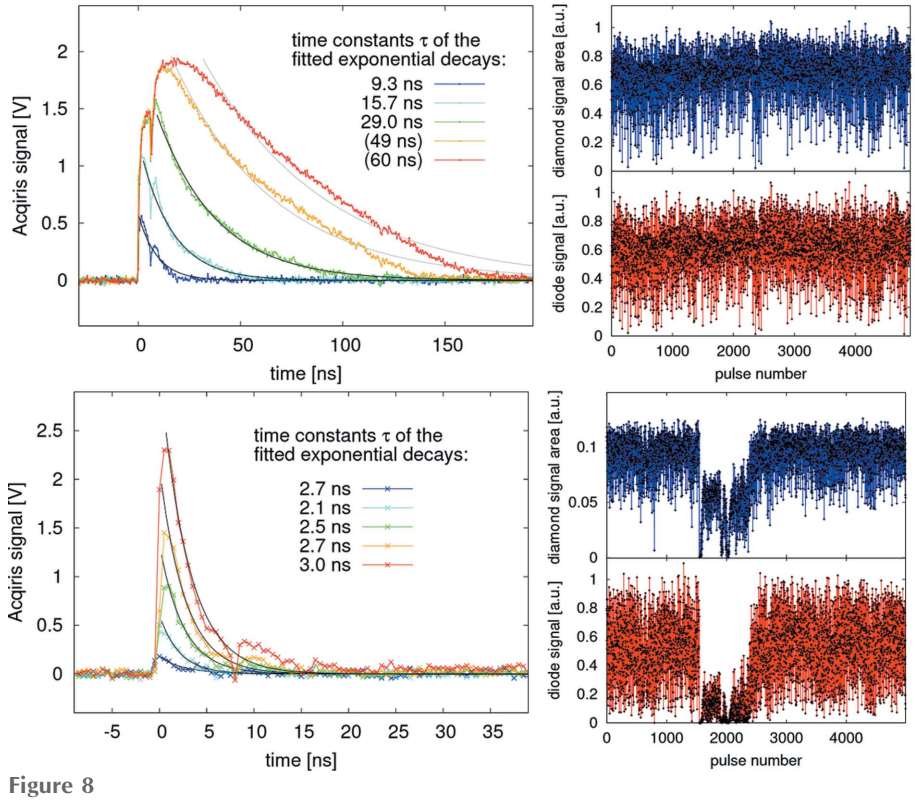

Figure 8
Left: selected individual traces of the Be electrode detector (top) and the graphite electrode detector (bottom). Note the different time scales. Right: integrated diamond detector signal (blue) for 5000 consecutive pulses compared with the integrated Si p-i-n diode monitor signal (red) for each of the two detectors: Be electrode detector (top) and graphite electrode detector (bottom).

time constant (Fig. 8, top left). The signal shape follows an exponential decay for weak and moderate pulses, but at higher photon intensities the shape starts deviating from this functional form. Pulses of higher intensity are of significant longer duration. We believe this behavior is caused mainly by a breakdown of the applied field that is screened by the large amount of charges created inside the diamond, outnumbering the stored charges responsible for the applied field. The collapse of that field reduces the drift velocities of holes and electrons [in fact it replaces the directed drift velocity in the presence of an electric field by a diffusive motion at thermal velocities, accidentally of similar magnitude (Ščajev *et al.*, 2013), but isotropic] and delays the charge collection. Fortunately, carrier lifetimes in scCVD diamond are much larger than the signal widths obtained here, so all charges are eventually detected nonetheless while the bias field is gradually restored.

The signal from the graphite electrode detector is very fast. After reaching the peak value the signal exhibits an exponential decay with a time constant in the range 2–3 ns (Fig. 8, bottom left), not significantly different from the ideal value of τ_{exp} = 1.4 ns. This short signal duration is surprising compared with the Be electrode detector because (*a*) the bias voltage is lower and (*b*) the thickness is larger and hence more charges should be created. We thus believe that the measured fast signal duration is in fact the consequence of the short charge-carrier lifetimes in heteroepitaxially grown diamond (possibly a few nanoseconds only). The recombination of charges is also visible in the analysis of the integrated signals (see below).

5.2. Detection efficiency

The integrated signal Q_{pulse} detected by the fast digitizer was very different for the two detectors, although the incoming flux was similar and the detector thicknesses only differ by a factor of about two, though the electric field generated by the bias voltage differed by a factor of four. We have

$$Q_{pulse} = (1/R_{measure}) \int U(t)\,dt \quad (4)$$

where $U(t)$ is measured by the digitizer (must be corrected by the −33 dB signal attenuation) and $R_{measure}$ = 50 Ω. Knowing Q_{pulse}, it is possible to calculate how many electron–hole (e-h) pairs are created, how many photons were detected and how many photons were incident on the detector per pulse:

$$N_{pulse}^{e\text{-}h} = \left(\frac{1}{e}\right) Q_{pulse}, \quad (5)$$

$$N_{pulse}^{absorbed} = \left(\frac{13\,eV}{E}\right) N_{pulse}^{e\text{-}h}, \quad (6)$$

$$N_{pulse}^{incident} = \left(\frac{1}{1-T}\right) N_{pulse}^{absorbed}. \quad (7)$$

The strongest pulse for the Be electrode detector (red curve, top left of Fig. 8) leads to Q_{pulse} = 141 nC and $N_{pulse}^{incident}$ = 3 × 10^{10}. Given the linac operation parameters, mirror transmission and the slit settings upstream of the detector, a photon flux of ∼7 × 10^{10} photons pulse^{-1} is expected according to estimates by LCLS. This is a rather good agreement. Better agreement is obtained when following rule-of-thumb estimates for the integrated signal of the four Si p-i-n diodes I_{array2}, which receive the scattered intensity of a 1 µm-thick Si_3N_4 foil. This detector has not been calibrated and we have to extrapolate from known values of a similar detector at the XPP beamline, using a different gain setting and a thinner scattering foil. The estimated flux in this case is 3.2 × 10^{10} photons for the strongest pulses.[1] The single in-air Si p-i-n diode, I_{Si3}, mounted adjacent to our diamond detector cannot be used for flux estimations, as it is collecting scattering from air and the vacuum window under ill-defined conditions.

The strongest curve for the graphite electrode detector (red curve, bottom left of Fig. 8) only integrates to Q_{pulse} = 13 nC, despite having a higher absorption due to its higher crystal thickness. We obtain $N_{pulse}^{incident}$ = 1.3 × 10^9, *i.e.* more than an order of magnitude below expectation. Obviously the initial signal height is insufficiently sampled at 0.5 ns and a much faster digitizer would be needed to resolve the peak. Also, the applied bias voltage was smaller than in the Be electrode case; an effect amplified by the larger crystal thickness, leading to a field strength of 1 V µm^{-1}. A better explanation for the missing collected charges would be, however, that the heteroepitaxially grown diamond exhibits smaller carrier lifetimes and hence a large part of the charges recombine before entering the detection circuit.

5.3. Bias voltage dependence

Although a complete charge collection in diamond can be obtained at voltages as low as ∼0.1 V µm^{-1} (Morse *et al.*, 2010; Pomorski *et al.*, 2005), and 0.2 V µm^{-1} was observed to be sufficient in the α-particle test with the Be-coated detector (see Fig. 4), the time behavior of the detector signal still varies with the bias voltage, until saturation of the drift velocity is reached below ∼10 V µm^{-1} (Pomorski *et al.*, 2006, 2008). The measurements with the graphite electrode detector have only been performed at a bias voltage of 100 V, thus almost exactly at 1 V µm^{-1}. The bias voltage of the Be detector was varied between 10 and 160 V (upper limit chosen for safety reasons). For each bias voltage, at least 6000 pulses were acquired and averaged over pulse groups that showed similar peak heights (see Fig. 9).

It is seen that, for the Be electrode diamond detector and for the intense X-ray pulses, a high bias voltage, *i.e.* at least 160 V, must be applied. This corresponds to 4 V µm^{-1}.

5.4. Linearity

Since the intensities of SASE pulses vary significantly it is difficult to use standard methods, such as beam attenuation

[1] The conversion factor for the XPP monitor using a 0.1 µm-thick Si_3N_4 foil and a gain setting with a 120 pF capacitor is 3 × 10^{11} photons per 1 V output of the charge-to-amplitude converter. During our measurement we used a 620 pF capacitor and a 1 µm-thick Si_3N_4 foil, obtaining up to 5.5 V in amplitude. This scales thus to about 3.2 × 10^{10} photons for the strongest pulses.

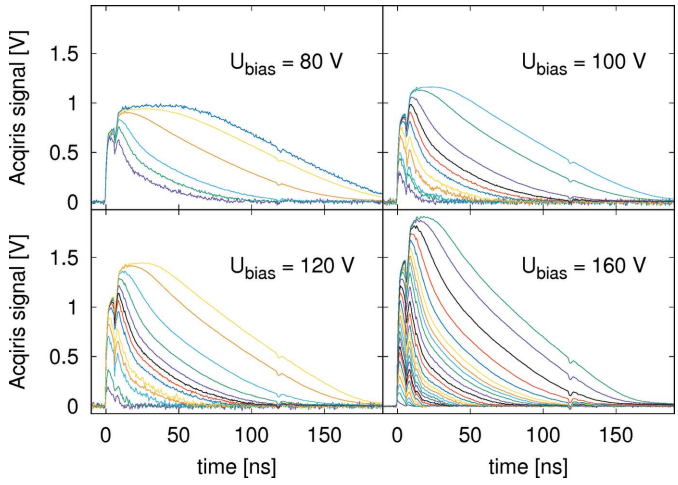

Figure 9
Signal from the diamond detector with Be electrodes. The figure shows typical shapes of the signal trace for different SASE pulse intensities, with four different applied bias voltages (80, 100, 120 and 160 V).

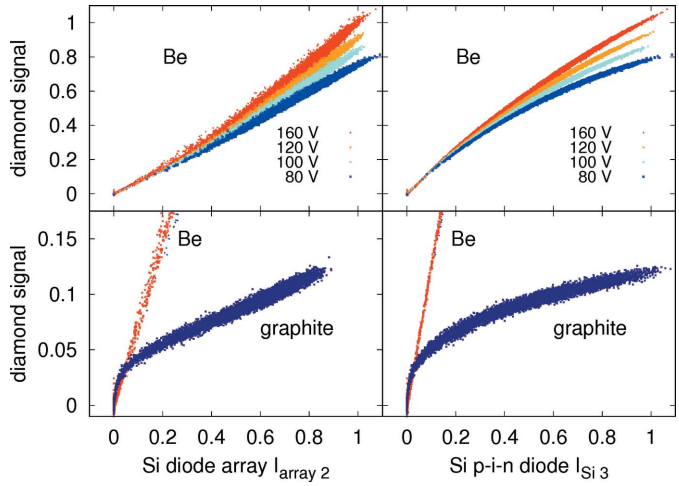

Figure 10
Correlation plot between the diamond detector signal and two different Si detectors: $I_{\rm array2}$ (left) and $I_{\rm Si3}$ (right). Top: Be electrode detector ($U_{\rm bias}$ = 160 V). Bottom: graphite electrode detector ($U_{\rm bias}$ = 100 V). The strongest signals correspond to about 3×10^{10} incident photons, as explained in §5.2.

with calibrated filters or slit size reduction, for a linearity check of the detectors. Instead, the integrated charge collected by the detector can be compared with the signal obtained from nearby Si p-i-n diodes monitors that are detecting scattered photons. In our experiment, the closest monitors were yielding $I_{\rm Si3}$ and $I_{\rm array2}$ as seen in Fig. 7. The signal of $I_{\rm Si3}$ is compared with the integrated signal of the Be electrode detector for 5000 pulses in Fig. 8 (top right) and of the graphite electrode detector in a similar way (bottom right) with the same scaling of all signals. For the Be electrode detector, a high similarity between the intensity detected in both detectors is observed. For the graphite electrode detector, a good correspondence is seen for the weakest signals (lower fringe of the 5000 pulses), whereas the higher edge of the graphite electrode detector in blue seems to vary less than the Si p-i-n diode in red (Fig. 8, bottom right).

Instead of tracing both signals as a function of pulse number, they can be visualized in a correlation plot, see Fig. 10, where each photon pulse is represented as a point in a $I_{\rm Si}$–$I_{\rm diamond}$ plot. The left-hand column uses $I_{\rm array2}$ and the right-hand column uses $I_{\rm Si3}$. The best correlation is seen between the Be electrode detector using a bias voltage of 160 V and the Si p-i-n diode $I_{\rm Si3}$ positioned in the vicinity of the diamond detector and detecting scattered radiation. Also, the Si p-i-n diode array $I_{\rm array2}$ does show a high degree of correlation with the Be electrode detector. The top row of Fig. 10 shows that the Be detector readout is better correlated to any of the two Si detectors than the Si detectors are correlated to each other, hence demonstrating its capacity as a high-precision monitor.

The graphite electrode signal seems to be linear with respect to the two Si detectors only for weak pulses, as seen in Fig. 10 (lower figures). The initial slope of the graphite detector is larger than the slope of the Be detector, which is understandable as it is a consequence of the larger diamond thickness. However, for slightly stronger pulses the signal detected with the graphite detector is much lower than expected. This is in agreement also with the fact that the calculated number of charges for a strong pulse is roughly one order of magnitude smaller than expected from the nominal photon flux. We explain this behavior by a limited charge carrier lifetime in the heteroepitaxially grown diamond, together with a limited bias voltage. For low-intensity pulses, the applied voltage is sufficient, so that the electric field does not break down inside the diamond and the created charges can be collected within the limited carrier lifetime. For higher-intensity pulses, the created charge is reducing the applied field, and the carrier collection time increases beyond the carrier lifetime.

For future experiments, the field strength inside the diamond needs to be increased by applying a higher bias voltage and the charge carrier lifetime of the diamond can be improved by a heteroepitaxial growth with a still lower dislocation density.

5.5. Position sensitivity

Despite the non-linear behavior of the graphite detector for strong SASE pulses it still offers the possibility of measuring the position of the incident beam with some precision.

Fig. 11 shows how the graphite electrode detector was wired in order to deliver current signals. The two signals I_1 and I_2 can be combined to yield position information $x_{\rm in}$ of the incident pulses, given *via*

$$x_{\rm in} = c\left(\frac{I_1 - I_2}{I_1 + I_2}\right), \tag{8}$$

where c is a constant that needs to be chosen properly to express $x_{\rm in}$ in a suitable scale like millimeters. The lower left-hand panel of Fig. 11 shows the magnitude of I_1 and I_2 as the detector is translated in the slit-defined beam (0.2 mm × 0.2 mm). The bias voltage was again 100 V. The rise of one signal as the respective electrode approaches the beam is obvious while the other signal is decreasing. However, the

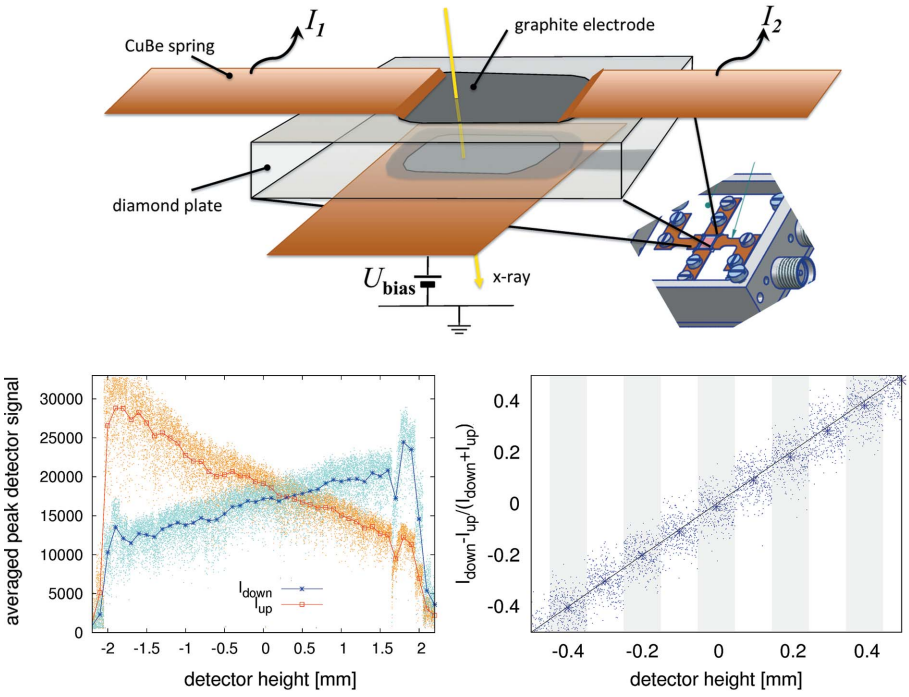

Figure 11
Position sensitivity of the graphite electrode detector. Top: wiring as a one-dimensional BPM. With the X-ray beam impinging as shown, I_1 will be higher than I_2. Left: $I_1 \rightarrow I_{down}$ in cyan, $I_2 \rightarrow I_{up}$ in orange. The individual pulse readouts are shown as points, and averages over 363 frames per detector position are displayed as red and blue lines. Right: calculated position shot per pulse (points) and average (line).

jitter in the beam's center position and intensity leads to strong variations in each of the signals. The lower right-hand panel shows x_{in}, as calculated using equation (8), for nine different detector heights. For each detector height, 363 pulses were collected and are plotted by individual small blue points. The average of the 363 points is shown in dark blue and lies well on the $y = x$ diagonal, as c was chosen properly.

Unfortunately, the individual points scatter over a region of 200 µm (the standard deviation is 65 µm), although a slit selected a 0.2 mm × 0.2 mm large region of a larger beam. It is therefore likely that this jitter has a big component from the detector itself in addition to a pointing instability of the incoming beam, but more conclusive tests need to be conducted. Again, a bias voltage higher than the applied 100 V might improve the results.

6. Conclusion and outlook

We have discussed the boundary conditions for the detection of hard X-ray FEL beam intensities using semi-transparent solid-state monitors. Diamond is the detector material of choice due to its outstanding thermal properties. Equally important is the ability of the electrodes to withstand the intense pulsed beams. We have manufactured and tested two custom-made detectors employing diamonds of different origin and with two different electrode materials, graphite and beryllium. The tests have been performed in the unfocused pink beam at the XCS station of LCLS. We found that the application of bias voltages and field strengths much larger than normally required for diamond detectors used in synchrotron X-ray beams is necessary to have a linear detector response in the FEL case. High bias voltages will maintain the electric field and allow rapid charge separation and collection before recombination, even with a very high number of charges created by the XFEL pulse. No beam damage was experienced in the experiment for either detector.

The Be electrode detector was slower than expected, but still capable of operating without pile-up at the 4.5 MHz frequency of the European XFEL. A higher bias voltage would accelerate the response of high-intensity pulses. The Be detector showed a very linear response with respect to the incoming varying pulse intensities. Fig. 10 demonstrates close correlation in read-out between the Be detector and the two Si detectors but it is not possible to determine which one is more linear from these correlation plots. If well characterized, corrections could probably be applied to make any of these intensity monitors linear over a wide range of pulse energies.

The graphite detector, on the other hand, is very fast, with a time constant in the range 2–3 ns. However, sufficient linearity was only observed for weak pulses indicating a limit in the number of collected charges. We explain this with a short carrier lifetime in the heteroepitaxially grown diamond and with a too low applied bias voltage U_{bias} during the experiment.

In order to stabilize the electric field in the diamond detector after the arrival of a high-intensity photon pulse, a backup capacitance could be wired in parallel to the detector (Griesmayer, 2015). This increases the capacitance C_{det} and should help in maintaining a high electric field for rapid charge collection. Unfortunately, this will also increase the detector time constant τ. However, for operation at the European XFEL, τ is allowed to reach about 40 ns, as seen in Fig. 2. The backup capacitance can then be designed accordingly,

$$C_{backup} = \frac{\tau_{target}}{R_{tot}} - C_{det}. \quad (9)$$

Further investigations of the limits in bias voltage and the optimum settings for XFEL applications are foreseen in the future. Possibly, scCVD diamond has a different breakdown voltage than heteroepitaxially grown diamond. In our experiments, the maximum values of the applied field were 4 V µm^{-1} and 1 V µm^{-1}, respectively, for the Be and graphite electrode detector. In the literature a breakdown field strength of 1000 V µm^{-1} is often used for calculations, *e.g.* of the figure of merit (Collins, 1994). In several recent studies on Schottky

diodes (Teraji *et al.*, 2007; Dutta *et al.*, 2016) and in earlier breakdown measurements on oriented diamond films on silicon (Hessmer *et al.*, 1994), maximum values of 1–1.5 MV cm^{-1} have been found. According to these reports, even bias voltages that could avoid a complete internal shielding of the electric field by the extremely high electron–hole pair densities encountered for the absorption of XFEL pulses should be applicable ($\sim$100 V µm^{-1}). However, in order to limit the absolute voltages that have to be handled, a detector thickness of 10 µm or lower would then be preferable.

Thinner diamond detectors for XFEL applications will be beneficial for many reasons: (*a*) less X-ray absorption, (*b*) less signal attenuation required, (*c*) less created charges inside the diamond and (*d*) a higher capacitance and thus more stored charges. However, τ will increase with thinner diamond so Be electrodes might be preferred over graphite. Unfortunately, Be is an unusual metal for electronics applications and can present a health risk. For example, it was difficult to find a partner for the wire-bonding between the Be electrode and the PCB. To ease the wire-bonding, diamond plates with lateral TiN contact pads reaching under the Be coating have been prepared for future detectors.

For many applications, a larger detector surface is desirable. This is possible using the heteroepitaxially grown diamond, and work on thinner large diamond plates for this application is ongoing. A further reduction of dislocation density in order to increase the charge carrier lifetimes is necessary and tests on the applicable voltage limits are to be performed. The structural and chemical nature of the hot spots needs investigation in order to avoid them during sample preparation, thereby achieving the most homogeneous response.

Diamond detectors in transmission may also be advantageous as monitors for weak (monochromatic) XFEL beams where detectors based on the detection of scattering can have very weak signals.

Acknowledgements

We thank K. de Hantsetters (Almax EasyLab, Belgium) and E. Graper (Lebow Company, USA) for providing the mask and beryllium coating of the diamond crystals. We thank C. Detlefs and the ESRF for access to test beam time.

Funding information

Funding for this research was provided by: US Department of Energy, Office of Science (award No. DE-AC02-76SF00515) for use of the Linac Coherent Light Source, SLAC National Accelerator Laboratory.

References

Alonso-Mori, R., Caronna, C., Chollet, M., Curtis, R., Damiani, D. S., Defever, J., Feng, Y., Flath, D. L., Glownia, J. M., Lee, S., Lemke, H. T., Nelson, S., Bong, E., Sikorski, M., Song, S., Srinivasan, V., Stefanescu, D., Zhu, D. & Robert, A. (2015). *J. Synchrotron Rad.* **22**, 508–513.

Altarelli, M. (2015). *High Power Laser Sci. Eng.* **3**, e18.

Antonelli, M., Di Fraia, M., Carrato, S., Cautero, G., Menk, R., Jark, W., Ganbold, T., Biasiol, G., Callegari, C., Coreno, M., De Sio, A. & Pace, E. (2013). *Nucl. Instrum. Methods Phys. Res. A*, **730**, 164–167.

Bionta, M. R. (2000). *Controlling Dose to Low-Z Solids at LCLS.* Technical Report. Lawrence Livermore National Laboratory, USA.

Bohon, J., Muller, E. & Smedley, J. (2010). *J. Synchrotron Rad.* **17**, 711–718.

Bonifacio, R., Pellegrini, C. & Narducci, L. M. (1984). *Opt. Commun.* **50**, 373–378.

Collins, A. T. (1994). *Properties and Growth of Diamond*, edited by G. Davies, p. 288. London: The Institution of Electrical Engineers.

De Sio, A., Pace, E., Cinque, G., Marcelli, A., Achard, J. & Tallaire, A. (2007). *Spectrochimica Acta B*, **62**, 558–561.

Desjardins, K., Pomorski, M. & Morse, J. (2014). *J. Synchrotron Rad.* **21**, 1217–1223.

Dutta, M., Koeck, F. A. M., Hathwar, R., Goodnick, S. M., Nemanich, R. J. & Chowdhury, S. (2016). *IEEE Electron Device Lett.* **37**, 1170–1173.

Emma, P., Holtkamp, N. R., Nuhn, H.-D., Arbelaez, D., Corlett, J. N., Myers, S. A., Prestemon, S., Schlueter, D., Doose, C. L., Fuerst, J. D., Gluskin, E., Hasse, Q. B., Ivanyushenkov, Y., Kasa, M., Pile, G. & Trakhtenberg, E. (2014). *Proceedings of the 36th International Free Electron Laser Conference*, 25–29 August 2014, Basel, Switzerland, p. 649. THA03.

Feng, Y., Feldkamp, J. M., Fritz, D. M., Cammarata, M., Aymeric, R., Caronna, C., Lemke, H. T., Zhu, D., Lee, S., Boutet, S., Williams, G., Tono, K., Yabashi, M. & Hastings, J. B. (2011). *Proc. SPIE*, **8140**, 81400Q.

Fraimovitch, D., Adelberd, A., Marunko, S., Lefeuvre, G. & Ruzin, A. (2016). *Nucl. Instrum. Methods Phys. Res. A*, **845**, 76–79.

Fuchs, M. R., Holldack, K., Bullough, M., Walsh, S., Wilburn, C., Erko, A., Schäfers, F. & Mueller, U. (2008). *Rev. Sci. Instrum.* **79**, 063103.

Gaudin, J., Medvedev, N., Chalupský, J., Burian, T., Dastjani-Farahani, S., Hájková, V., Harmand, M., Jeschke, H. O., Juha, L., Jurek, M. & Klinger, D. (2013). *Phys. Rev. B*, **88**, 060101.

Griesmayer, E. (2015). Private communication.

Hau-Riege, S. P., Bionta, R. M., Ryutov, D. D. & Krzywinski, J. (2008). *J. Appl. Phys.* **103**, 053306.

Hau-Riege, S. P., London, R. A., Bionta, R. M., McKernan, M. A., Baker, S. L., Krzywinski, J., Sobierajski, R., Nietubyc, R., Pelka, J. B., Jurek, M., Juha, L., Chalupský, J., Cihelka, J., Hájková, V., Velyhan, A., Krása, J., Kuba, J., Tiedtke, K., Toleikis, S., Tschentscher, T., Wabnitz, H., Bergh, M., Caleman, C., Sokolowski-Tinten, K., Stojanovic, N. & Zastrau, U. (2007). *Appl. Phys. Lett.* **90**, 173128.

Hau-Riege, S. P., London, R. A., Graf, A., Baker, S. L., Soufli, R., Sobierajski, R., Burian, T., Chalupsky, J., Juha, L., Gaudin, J., Krzywinski, J., Moeller, S., Messerschmidt, M., Bozek, J. & Bostedt, C. (2010). *Opt. Express*, **18**, 23933–23938.

Herrmann, S., Hart, P., Freytag, M., Pines, J., Weaver, M., Sapozhnikov, L., Nelson, S., Koglin, J., Carini, G. A., Tomada, A. & Haller, G. (2014). *J. Phys. Conf. Ser.* **493**, 012014.

Hessmer, R., Schreck, M., Geier, S. & Stritzker, B. (1994). *Diamond Relat. Mater.* **3**, 951–956.

Isberg, J., Hammersberg, J., Johansson, E., Wikström, T., Twitchen, D. J., Whitehead, A. J., Coe, S. E. & Scarsbrook, G. A. (2002). *Science*, **297**, 1670–1672.

Kalish, R. & Prawer, S. (1995). *Nucl. Instrum. Methods Phys. Res. B*, **106**, 492–499.

Keister, J. W. & Smedley, J. (2009). *Nucl. Instrum. Methods Phys. Res. A*, **606**, 774–779.

Keister, J. W., Smedley, J., Muller, E. M., Bohon, J. & Héroux, A. (2011). *Nucl. Instrum. Methods Phys. Res. A*, **649**, 91–93.

Komlenok, M., Bolshakov, A., Ralchenko, V., Konov, V., Conte, G., Girolami, M., Oliva, P. & Salvatori, S. (2016). *Nucl. Instrum. Methods Phys. Res. A*, **837**, 136–142.
Kondratenko, A. M. & Saldin, E. L. (1980). *Part. Accel.* **10**, 207–216.
Koyama, T., Yumoto, H., Senba, Y., Tono, K., Sato, T., Togashi, T., Inubushi, Y., Katayama, T., Kim, J., Matsuyama, S., Mimura, H., Yabashi, M., Yamauchi, K., Ohashi, H. & Ishikawa, T. (2013*a*). *Opt. Express*, **21**, 15382–15388.
Koyama, T., Yumoto, H., Senba, Y., Tono, K., Sato, T., Togashi, T., Inubushi, Y., Kim, J., Kimura, T., Matsuyama, S., Mimura, H., Yabashi, M., Yamauchi, K., Ohashi, H. & Ishikawa, T. (2013*b*). *J. Phys. Conf. Ser.* **463**, 012043.
Kudo, T., Tono, K., Yabashi, M., Togashi, T., Sato, T., Inubushi, Y., Omodani, M., Kirihara, Y., Matsushita, T., Kobayashi, K., Yamaga, M., Uchiyama, S. & Hatsui, T. (2012). *Rev. Sci. Instrum.* **83**, 043108.
London, R. A., Bionta, R. M., Tatchyn, R. O. & Roesler, S. (2001). *Proc. SPIE*, **4500**, 51–62.
Madsen, A., Hallmann, J., Roth, T. & Ansaldi, G. (2013). Technical Design Report XFEL.EU TR-2013-005. European XFEL, Hamburg, Germany.
Mayr, M., Ščajev, P. & Schreck, M. (2018). In preparation.
Medvedev, N., Jeschke, H. O. & Ziaja, B. (2013*a*). *Phys. Rev. B*, **88**, 224304.
Medvedev, N., Jeschke, H. O. & Ziaja, B. (2013*b*). *New J. Phys.* **15**, 015016.
Medvedev, N., Li, Z. & Ziaja, B. (2015). *Phys. Rev. B*, **91**, 054113.
Morse, J., Salomé, M., Berdermann, E., Pomorski, M., Cunningham, W. & Grant, J. (2007). *Diamond Relat. Mater.* **16**, 1049–1052.
Morse, J., Solar, B. & Graafsma, H. (2010). *J. Synchrotron Rad.* **17**, 456–464.
Pomorski, M. (2008). PhD thesis, Johann Wolfgang Goethe Universität, Frankfurt, Germany.
Pomorski, M., Berdermann, E., Caragheorgheopol, A., Ciobanu, M., Kiš, M., Martemiyanov, A., Nebel, C. & Moritz, P. (2006). *Phys. Status Solidi A*, **203**, 3152–3160.
Pomorski, M., Berdermann, E., Ciobanu, M., Martemyianov, A., Moritz, P., Rebisz, M. & Marczewska, B. (2005). *Phys. Status Solidi A*, **202**, 2199–2205.
Pomorski, M., Berdermann, E., de Boer, W., Furgeri, A., Sander, C. & Morse, J. (2007). *Diamond Relat. Mater.* **16**, 1066–1069.
Pomorski, M., Ciobanu, M., Mer, C., Rebisz-Pomorska, M., Tromson, D. & Bergonzo, P. (2009). *Phys. Status Solidi A*, **206**, 2109–2114.
Robert, A., Curtis, R., Flath, D., Gray, A., Sikorski, M., Song, S., Srinivasan, V. & Stefanescu, D. (2013). *J. Phys. Conf. Ser.* **425**, 212009.
Ščajev, P., Gudelis, V., Tallaire, A., Barjon, J. & Jarašiūnas, K. (2013). *Phys. Status Solidi A*, **210**, 2016–2021.
Schreck, M. (2014). *Comprehensive Hard Materials*, edited by V. K. Sarin, pp. 269–304. Oxford: Elsevier.
Shimaoka, T., Kaneko, J. H., Tsubota, M., Shimmyo, H., Watanabe, H., Chayahara, A., Umezawa, H. & Shikata, S. (2016). *Europhys. Lett.* **113**, 62001.
Stehl, C., Fischer, M., Gsell, S., Berdermann, E., Rahman, M. S., Traeger, M., Klein, O. & Schreck, M. (2013). *Appl. Phys. Lett.* **103**, 151905.
Tachibana, T. & Glass, J. T. (1995). *Diamond: Electronic Properties and Applications*, edited by L. S. Pan and D. R. Kania, *Kluwer International Series in Engineering and Computer Science*, pp. 319–348. New York: Springer.
Tavella, F., Höppner, H., Tkachenko, V., Medvedev, N., Capotondi, F., Golz, T., Kai, Y., Manfredda, M., Pedersoli, E., Prandolini, M. J., Stojanovic, N., Tanikawa, T., Teubner, U., Toleikis, S. & Ziaja, B. (2017). *High Energy Density Phys.* **24**, 22–27.
Teraji, T., Koizumi, S., Koide, Y. & Ito, T. (2007). *Jpn. J. Appl. Phys.* **46**, L196–L198.
Tiedtke, K., Feldhaus, J., Hahn, U., Jastrow, U., Nunez, T., Tschentscher, T., Bobashev, S. V., Sorokin, A. A., Hastings, J. B., Möller, S., Cibik, L., Gottwald, A., Hoehl, A., Kroth, U., Krumrey, M., Schöppe, H., Ulm, G. & Richter, M. (2008). *J. Appl. Phys.* **103**, 094511.
Tono, K., Kudo, T., Yabashi, M., Tachibana, T., Feng, Y., Fritz, D., Hastings, J. & Ishikawa, T. (2011). *Rev. Sci. Instrum.* **82**, 023108.
Wort, C. J. H. & Balmer, R. S. (2008). *Mater. Today*, **11**, 22–28.
Zhou, T., Ding, W., Gaowei, M., De Geronimo, G., Bohon, J., Smedley, J. & Muller, E. (2015). *J. Synchrotron Rad.* **22**, 1396–1402.